

Detailed multiwavelength modelling of the dark GRB 140713A and its host galaxy

A. B. Higgins¹,^{1*} A. J. van der Horst,^{2,3} R. L. C. Starling,¹ G. Anderson^{4,5},
D. Perley⁶,⁶ H. van Eerten,⁷ K. Wiersema,⁸ P. Jakobsson,⁹ C. Kouveliotou,²
G. P. Lamb¹ and N. R. Tanvir¹

¹Department of Physics and Astronomy, University of Leicester, University Road, Leicester LE1 7RH, UK

²Department of Physics, The George Washington University, 725 21st Street NW, Washington, DC 20052, USA

³Astronomy, Physics, and Statistics Institute of Sciences (APSIS), 725 21st Street NW, Washington, DC 20052, USA

⁴International Centre for Radio Astronomy Research, Curtin University, GPO Box U1987, Perth, WA 6845, Australia

⁵Department of Physics and Astrophysics, University of Oxford, Denys Wilkinson Building, Oxford OX1 3RH, UK

⁶Astrophysics Research Institute, LJMU, IC2, Liverpool Science Park, 146 Brownlow Hill, Liverpool L3 5RF, UK

⁷Department of Physics, University of Bath, Claverton Down, Bath BA2 7AY, UK

⁸Department of Physics, University of Warwick, Coventry CV4 7AL, UK

⁹Centre for Astrophysics and Cosmology, Science Institute, University of Iceland, Dunhagi 5, 107 Reykjavik, Iceland

Accepted 2019 February 5. Received 2019 February 1; in original form 2018 November 16

ABSTRACT

We investigate the afterglow of GRB 140713A, a gamma-ray burst (GRB) that was detected and relatively well sampled at X-ray and radio wavelengths, but was not present at optical and near-infrared wavelengths, despite searches to deep limits. We present the emission spectrum of the likely host galaxy at $z = 0.935$ ruling out a high-redshift explanation for the absence of the optical flux detection. Modelling the GRB multiwavelength afterglow using the radiative transfer hydrodynamics code BOXFIT provides constraints on physical parameters of the GRB jet and its environment, for instance a relatively wide jet opening angle and an electron energy distribution slope p below 2. Most importantly, the model predicts an optical flux about two orders of magnitude above the observed limits. We calculated that the required host extinction to explain the observed limits in the r , i , and z bands was $A_V^{\text{host}} > 3.2$ mag, equivalent to $E(B - V)^{\text{host}} > 1.0$ mag. From the X-ray absorption we derive that the GRB host extinction is $A_V^{\text{host}} = 11.6_{-5.3}^{+7.5}$ mag, equivalent to $E(B - V)^{\text{host}} = 3.7_{-1.7}^{+2.4}$ mag, which is consistent with the extinction required from our BOXFIT derived fluxes. We conclude that the origin of the optical darkness is a high level of extinction in the line of sight to the GRB, most likely within the GRB host galaxy.

Key words: gamma-ray burst: individual: GRB140713A.

1 INTRODUCTION

Gamma-ray bursts (GRBs) are short-lived, explosive transients that can be detected at multiple wavelengths. The prompt gamma-ray emission is likely caused by internal shocks of material accelerated to relativistic speeds with a range of Lorentz factors (Rees & Meszaros 1994). The afterglow, produced when the relativistic ejecta shock into the surrounding medium (Piran 1999; Zhang & Mészáros 2004; Kumar & Zhang 2015; Schady 2017; van Eerten 2018), lasts longer and produces broad-band emission ranging from X-ray to radio wavelengths. Observing the multiwavelength

emission of the afterglow can be used to study the interaction of a GRB with its environment.

Some GRBs detected at X-ray and radio wavelengths have lower than expected fluxes or deep limits in the optical bands. These are referred to as ‘dark’ bursts, the earliest documented being GRB 970828 (Groot et al. 1998). This suppression of optical flux can have a variety of causes. At high redshifts, the most likely cause for the optical darkness is Lyman α absorption occurring at $\lambda_{\text{obs}} < 1216(1 + z)\text{Å}$ (Tanvir et al. 2009; Cucchiara et al. 2011). If the GRBs reside at lower redshifts, the observed optical darkness may result from a number of possibilities. Extinction due to line-of-sight dust contributions from the host, our Galaxy and the interstellar medium (ISM) can highly obscure the rest-frame optical flux of GRBs. A previous investigation by Perley et al. (2009) observing 29 host galaxies of dark GRBs concluded that

* E-mail: abh13@le.ac.uk

a significant fraction of hosts (six out of 22 with estimated dust extinction) had a moderately high level of extinction ($A_V^{\text{host}} > 0.8$ mag). Furthermore, some dark bursts appear to reside in hosts with very high extinction (e.g. GRB 111215A where $A_V^{\text{host}} > 7.5$ mag; Zauderer et al. 2013; van der Horst et al. 2015). As GRBs trace cosmic star formation through their high energy emission (Perley et al. 2016), and a significant fraction of star formation is dust-obscured, dark GRBs may provide a way to investigate dust-obscured star formation (Blain & Natarajan 2000; Ramirez-Ruiz, Trentham & Blain 2002). It is also possible that a GRB has either a low-luminosity or low-frequency synchrotron cooling break, and the subsequent afterglow would not have produced an optical flux that was detectable due to current instrument sensitivity or optical follow-up that simply was not deep enough. Coupled with a moderate extinction, many dark GRBs may not have been detectable in the optical at all.

The launch of NASA’s Neil Gehrels Swift Observatory (*Swift*; Gehrels et al. 2004) satellite in 2004 allowed rapid, follow-up observations of GRB afterglows. This has given us unprecedented multiwavelength coverage of GRBs that was not possible previously. The percentage of GRBs found by the *Swift* Burst Alert Telescope (BAT; Barthelmy et al. 2005) and additionally detected by the X-ray telescope (XRT; Burrows et al. 2005) stands at > 90 per cent (Burrows et al. 2008; Evans et al. 2009; *Swift* GRB table¹). The *Swift* Ultraviolet/Optical Telescope (Roming et al. 2005) has detected an optical afterglow candidate in ~ 30 per cent of *Swift*/BAT detected GRBs (Roming et al. 2009, *Swift* GRB table¹).

A number of investigations complementing *Swift* XRT detections with optical follow-up have been undertaken (e.g. Fynbo et al. 2009; Greiner et al. 2011; Melandri et al. 2012). These samples differ in selection criteria but estimates have shown that dark bursts may account for 25–40 per cent of the *Swift* GRB population.

Several methods have been proposed to classify these so-called dark bursts, comparing the X-ray afterglow properties to the optical/nIR upper limits. Rol et al. (2005) estimated a minimum optical flux by extrapolating from the X-ray flux using both temporal and spectral information, assuming a synchrotron spectrum. Jakobsson et al. (2004) and van der Horst et al. (2009) characterize ‘thresholds’ to classify a dark GRB using the optical-to-X-ray spectral index. These comparisons can only be used provided the observations used are made several hours after the GRB onset. Jakobsson et al. (2004) and van der Horst et al. (2009) highlight that classifications using spectral slopes alone may not fully determine whether a burst is truly dark, suggesting that these thresholds should only be used as quick diagnostic tools. They suggest that dark bursts should be modelled individually to fully characterize their nature. If multiwavelength data are available (i.e. radio and X-ray), broad-band modelling can be used to estimate the expected optical fluxes to determine the host galaxy optical extinction (discussed in van der Horst et al. 2015). Some dark GRBs with well-sampled data at both the X-ray and radio wavelengths have been studied in detail; GRB 020819 (Jakobsson et al. 2005), GRB 051022 (Castro-Tirado et al. 2007; Rol et al. 2007), GRB 110709B (Zauderer et al. 2013), and GRB 111215A (Zauderer et al. 2013; van der Horst et al. 2015). However, this sample is still small and highlights the importance to analyse new dark bursts to investigate the properties of the burst, the origin of the optical darkness and the use of dark GRBs as probes of dust obscured star formation.

We investigate GRB 140713A, a burst discovered by *Swift* (Mangano et al. 2014) and *Fermi*/GBM (Zhang 2014). GRB 140713A was a long-duration burst with a $T_{90} \sim 5$ s (15–350 keV) and a fluence $F_\gamma = 3.7(\pm 0.3) \times 10^{-7}$ erg cm⁻² (15–150 keV; Stamatikos et al. 2014). An X-ray counterpart was detected by the *Swift*/XRT with initial localization uncertainty of 2 arcsec (90 per cent containment; Beardmore et al. 2014) though this was later improved to 1.4 arcsec² (90 per cent containment). A radio counterpart was also detected at 15.7 GHz with the Arcminute Microkelvin Imager (AMI) Large Array (Anderson et al. 2014) coincident with the *Swift*/XRT position. A potential host galaxy was found with the 10.4 m Gran Telescopio Canarias (GTC; Castro-Tirado et al. 2014). We model the multiwavelength afterglow data using numerical modelling based on hydrodynamical jet simulations – the first time this has been attempted on an optically dark GRB. The modelling can estimate the optical flux we would expect from the GRB and can be used to investigate the origin of the optical darkness.

2 OBSERVATIONS AND DATA ANALYSIS

2.1 Radio observations

We observed GRB 140713A from 2014 July 13 to October 2 with the Large Array of the AMI interferometer (Zwart et al. 2008) at a central frequency of 15.7 GHz (between 13.9 and 17.5 GHz), and with WSRT at 1.4 and 4.8 GHz. The AMI observations were taken as part of the AMI Large Array Rapid-Response Mode program, which is designed to probe the early-time radio properties of transient events by automatically responding to transient alert notices (Staley et al. 2013; Staley & Fender 2016; Anderson et al. 2018). On responding to the *Swift*/BAT trigger of GRB 140713A, AMI was observing the event within 6 min for 2 h, obtaining a 3σ flux upper limit of 0.27 mJy. Follow-up observations were manually scheduled and obtained every few days for over 2 months, with the first confirmed detection occurring 3.19 d post-burst (Anderson et al. 2018). AMI data were reduced using the AMISURVEY software package (Staley & Anderson 2015c), which utilizes the AMI specific data reduction software AMI-REDUCE (Dickinson et al. 2004) and CHIMENEA, which is built upon the Common Astronomy Software Application (Jaeger 2008) package and specifically designed to clean and image multi-epoch transient data (Staley & Anderson 2015a,b). All flux densities were measured using the Low-Frequency Array Transient Pipeline (TRAP; Swinbank et al. 2015) and the quoted flux errors were calculated using the quadratic sum of the error output by TRAP and the 5 per cent flux calibration error of AMI (Perrott et al. 2013). For further details on the reduction and analysis we performed on the AMI observations, see Anderson et al. (2018).

In our WSRT observations, we used the Multi Frequency Front Ends (Tan 1991) in combination with the IVC + DZB back end in continuum mode, with a bandwidth of 8×20 MHz at all observing frequencies. Gain and phase calibrations were performed with the calibrator 3C 286 for all observations. The observations were analysed using the Multichannel Image Reconstruction Image Analysis and Display (Sault, Teuben & Wright 1995) software package. There were multiple detections at 4.8 GHz, while the 1.4 GHz observation at 25 d resulted in a non-detection. An observation at 1.4 GHz with the Giant Metrewave Radio Telescope (GMRT), 11 d after the burst, also resulted in a non-detection (Chandra & Nayana 2014). The radio data sets can be seen in Table 1 and the light

¹https://swift.gsfc.nasa.gov/archive/grb_table/

²http://www.swift.ac.uk/xrt_positions/

Table 1. AMI and WSRT observations of GRB 140713A where ΔT is the mid-point of each observation in days after the GRB trigger time. Non-detections are given as 3σ upper limits. The AMI data are identical to those quoted in Anderson et al. (2018).

Epoch	ΔT (d)	Integration time (h)	Observatory	Frequency (GHz)	Flux (μJy)
Jul 13.784–13.867	0.05	2.0	AMI	15.7	<270
Jul 14.791–14.958	1.09	4.0	AMI	15.7	<180
Jul 16.884–17.050	3.18	4.0	AMI	15.7	600(\pm 90)
Jul 17.858–18.024	4.16	4.0	AMI	15.7	<270
Jul 18.793–18.959	5.09	4.0	AMI	15.7	780(\pm 90)
Jul 19.687–20.185	6.15	12.0	WSRT	4.8	<96
Jul 19.936–20.102	6.24	4.0	AMI	15.7	840(\pm 70)
Jul 20.943–21.109	7.24	4.0	AMI	15.7	820(\pm 90)
Jul 22.921–23.087	9.22	4.0	AMI	15.7	1370(\pm 80)
Jul 24.673–25.172	11.16	12.0	WSRT	4.8	189(\pm 34)
Jul 24.860–25.027	11.16	4.0	AMI	15.7	1310(\pm 100)
Jul 26.894–27.061	13.18	4.0	AMI	15.7	1650(\pm 100)
Jul 28.784–28.950	15.08	4.0	AMI	15.7	870(\pm 70)
Jul 30.657–31.155	17.11	12.0	WSRT	4.8	205(\pm 28)
Jul 30.807–30.973	17.11	4.0	AMI	15.7	690(\pm 70)
Aug 1.859–2.025	19.16	4.0	AMI	15.7	890(\pm 70)
Aug 3.860–4.026	21.16	4.0	AMI	15.7	1050(\pm 70)
Aug 5.815–5.981	23.12	4.0	AMI	15.7	700(\pm 70)
Aug 6.838–7.136	24.11	12.0	WSRT	4.8	137(\pm 31)
Aug 6.868–7.034	24.17	4.0	AMI	15.7	790(\pm 60)
Aug 7.635–8.133	25.10	12.0	GMRT	1.4	<225
Aug 12.792–12.917	30.07	3.0	AMI	15.7	710(\pm 70)
Aug 14.871–14.995	32.15	3.0	AMI	15.7	530(\pm 70)
Aug 16.870–18.947	34.13	2.0	AMI	15.7	400(\pm 60)
Aug 18.605–19.103	36.07	12.0	WSRT	4.8	189(\pm 32)
Aug 18.781–18.947	36.08	4.0	AMI	15.7	490(\pm 70)
Aug 20.786–20.869	38.05	2.0	AMI	15.7	<180
Aug 23.726–28.014	41.03	4.0	AMI	15.7	350(\pm 50)
Aug 27.848–28.014	45.15	4.0	AMI	15.7	290(\pm 40)
Aug 29.823–29.989	47.12	4.0	AMI	15.7	270(\pm 50)
Aug 31.757–31.832	49.01	1.8	AMI	15.7	<210
Sep 1.795–1.962	50.09	4.0	AMI	15.7	320(\pm 80)
Sep 2.596–3.062	51.05	12.0	WSRT	4.8	182(\pm 36)
Sep 2.683–2.928	51.02	5.9	AMI	15.7	180(\pm 40)
Sep 5.754–5.919	54.05	4.0	AMI	15.7	<120
Sep 7.778–7.942	56.08	3.9	AMI	15.7	<210
Sep 10.798–10.965	59.10	4.0	AMI	15.7	210(\pm 50)
Sep 14.716–14.882	63.02	4.0	AMI	15.7	<150
Sep 17.543–18.021	66.00	12.0	WSRT	4.8	192(\pm 38)
Sep 17.658–17.899	66.00	5.8	AMI	15.7	<90
Sep 23.766–23.932	72.07	4.0	AMI	15.7	<120
Oct 2.482–2.980	80.95	12.0	WSRT	4.8	127(\pm 32)
Oct 2.590–2.833	80.93	5.8	AMI	15.7	<150

curves are shown in Fig. 1. The 15.7 GHz data exhibits signs of scintillation, noticeable at time-scales of up to 2 weeks post-GRB.

2.2 Optical afterglow observations

We observed the field of GRB 140713A with the 2.5 m Nordic Optical Telescope (NOT) equipped with ALFOSC starting at 22:02 UT on 2014 July 13 (Cano, Malesani & Nielsen 2014). We obtained 5×180 s frames in both r and i , and 5×300 s in z . The NOT images have been calibrated to the USNO-B1 catalogue, using five stars in the field of view of GRB 140713A. The B_2 -, R_2 - and I -band magnitudes of the five stars have been transformed into SDSS filters r , i , and z (in the AB system) using the transformation equations in Jordi, Grebel & Ammon (2006). No object was detected within the XRT

error circle of the GRB, and we find 3σ upper limits for an isolated point source in our images of $r > 24.30$, $i > 23.50$, and $z > 22.60$, at 0.1454, 0.1585, and 0.1738 d after the burst onset, respectively. The uncertainties associated with these upper limits are $r = 0.16$ mag, $i = 0.15$ mag, and $z = 0.13$ mag, which includes the standard deviation of the average offset between the instrumental and USNO-B1 catalogue magnitudes, and the variance of the transformation equations, which have been added in quadrature. The optical limits were converted into flux density and are shown in Fig. 1.

2.3 Host galaxy observations and redshift determination

While no optical afterglow detection was reported for this burst, the presence of a compact, non-varying source within the XRT circle

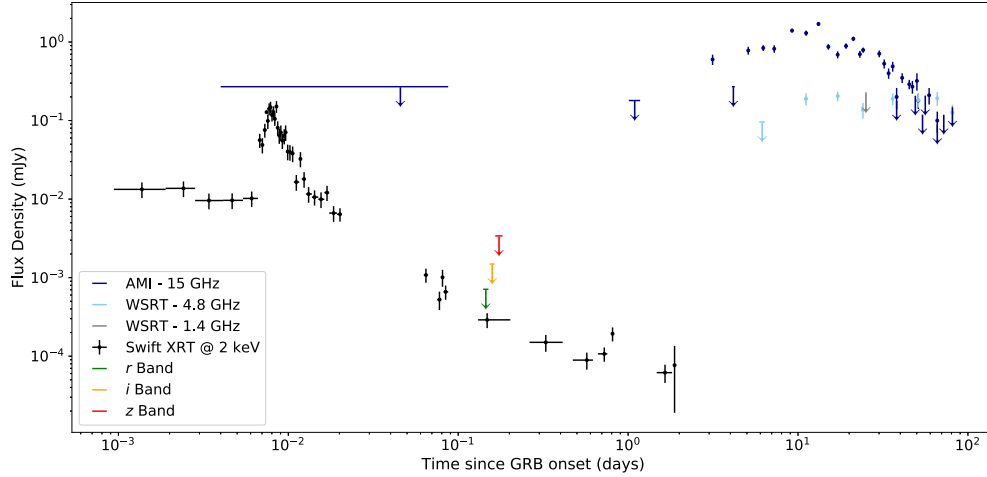


Figure 1. Time evolution of GRB 140713A at radio and X-ray wavelengths. The flux density detection errors quoted are 1σ and the non-detections are given as 3σ upper limits. The r , i , and z optical upper limits are also plotted. The X-ray flux density is derived from the unabsorbed flux values.

with $R \sim 24$ mag was first noted by Castro-Tirado et al. (2014) and proposed as a potential host galaxy.

To test the likelihood of finding an unrelated galaxy within the XRT error circle of GRB 140713A, we use the following relation (Bloom, Kulkarni & Djorgovski 2002)

$$P_{\text{chance}} = 1 - e^{-\pi r^2 \sigma(\leq m_R)}, \quad (1)$$

where r is the radius of the localization error circle and $\sigma(\leq m_R)$ is the expected number of galaxies per arcsec² brighter than a given R -band magnitude limit. Bloom et al. (2002) state that if $P_{\text{chance}} < 0.1$, the observed galaxy within the XRT error circle is most probably the host. Using the XRT error radius of 1.4 arcsec (90 per cent containment) and $m_R = 24$ mag we find $P_{\text{chance}} = 0.028$, providing further evidence that this galaxy is the probable GRB host.

We obtained both imaging and spectroscopy of this source with the Low Resolution Imaging Spectrometer (LRIS; Oke et al. 1995) on the Keck I 10 m telescope at Maunakea, on the nights of 2014 August 30 and 31. Imaging was obtained in a variety of filters and totalled 480 s in each of U band, g band, and i band, and 640 s with the long-pass RG850 filter (similar to SDSS z band). Images were reduced using the custom LPIPE pipeline and stacked. Photometric calibration was performed using both Landolt standards acquired during the night and (for filters other than U) PS1 secondary standards in the field, and consistent results were obtained. Additionally, the source was observed by IRAC on-board the *Spitzer* Space Telescope on 2016 November 8. We performed aperture photometry on the source within IDL, using a 1.5 arcsec aperture for optical filters and a 2.4 arcsec aperture for IRAC. Photometry is provided in Table 2 and uncertainties are approximate, dominated by the photometric calibration.

Our spectroscopic integration totalled approximately 1200 s (2×600 s blue, 2×590 s red) and employed the 400/3400 grism and 400/8500 grating on LRIS, covering a continuous wavelength range from the atmospheric cut-off to 10 290 Å. The reduced 1D spectrum (Fig. 2) shows two strong emission features at wavelengths corresponding to [O II] λ 3727 and [O III] λ 5007 at a common redshift of $z = 0.935$, identifying this as the redshift of the system.

We performed an SED fit to our photometry (as well as the R -band point from Castro-Tirado et al. 2014 – see Table 2) using our custom SED analysis software (Perley et al. 2013) assuming a star formation history that is constant from $z = 20$ to the observed

Table 2. Host galaxy photometry performed using a variety of filters and instruments.

Filter	Magnitude (AB)	Instrument
u	24.30 ± 0.20	Keck/LRIS
g	24.22 ± 0.10	Keck/LRIS
R	24.00 ± 0.50	GTC/OSIRIS
i	23.11 ± 0.10	Keck/LRIS
z	22.49 ± 0.10	Keck/LRIS
3.6	21.45 ± 0.05	Spitzer/IRAC
4.5	21.82 ± 0.05	Spitzer/IRAC

Note. Magnitudes are not corrected for Galactic extinction; $E(B - V) = 0.05$ (Schlafly & Finkbeiner 2011).

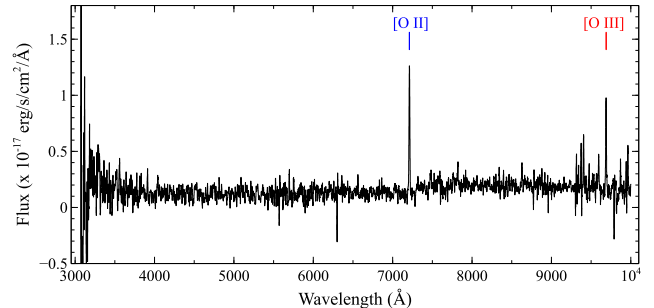


Figure 2. The LRIS host galaxy spectrum. Highlighted are the [O II] doublet (blue) and the [O III] λ 5007 (red) emission lines at a common redshift of $z = 0.935$. The spectrum was smoothed with a 5 pixel boxcar for display purposes.

redshift, except for an impulsive change at one point in the past. We found an excellent fit to a model with a total stellar mass of $2.2 \times 10^{10} M_{\odot}$ and a current star formation rate of $1.2 M_{\odot} \text{ yr}^{-1}$ (see Fig. 3). These values are typical of dark GRB hosts at similar redshift (Perley et al. 2013) and generally of optically selected galaxies at this epoch (Contini et al. 2012).

2.4 X-ray afterglow observations

The *Swift* satellite observed GRB 140713A with the XRT starting at 18:45 UT on 2014 July 13, ~ 80 s after the *Swift*/BAT trigger

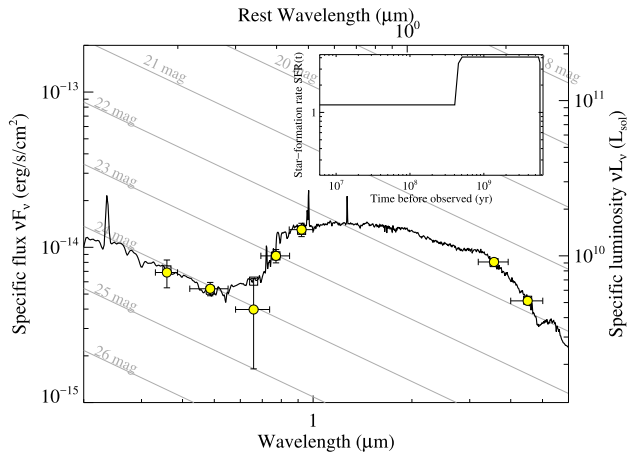


Figure 3. SED of the potential host galaxy of GRB 140713A. The data points are plotted in yellow (see Table 2), the best-fitting model is denoted by the solid black line. The inset shows the assumed star formation history prior to the galaxy redshift.

(Mangano et al. 2014). A coincident source was detected by the XRT and observations continued until ~ 163 ks after the *Swift*/BAT trigger for a total exposure time of 15.7 ks.

The X-ray light curve of GRB 140713A exhibits flaring ~ 500 s after the *Swift*/BAT trigger with a duration of ~ 1000 s (taken from UKSSDC XRT GRB catalogue; Evans et al. 2009). The flaring most probably arises from extended central engine activity. As we only investigated emission from the afterglow we excluded the first 1500 s of X-ray data in our modelling and only consider the later time X-ray emission. We performed spectral analysis of the late-time spectral data using XSPEC (v12.9; Arnaud 1996). We fit the data using an absorbed power law with a redshifted absorption component and a Galactic column density of $N_{\text{H,Gal}} = 4.97 \times 10^{20} \text{ cm}^{-2}$, calculated using the method described in Willingale et al. (2013). Using a Solar metallicity absorber (Z_{\odot}) at $z = 0.935$, we found a photon index $\Gamma = 1.83^{+0.37}_{-0.33}$ and an excess intrinsic column density, $N_{\text{H,host}} = 2.56^{+1.48}_{-1.12} \times 10^{22} \text{ cm}^{-2}$ (90 per cent confidence; C-stat = 114 for 155 degrees of freedom). GRB hosts typically have metallicities that differ from Solar metallicity (Schady et al. 2012), so we also fit the data using LMC-like ($Z_{\odot}/3$) and SMC-like ($Z_{\odot}/8$) metallicities at $z = 0.935$ where Z_{\odot} is Solar metallicity. We found photon indices of $\Gamma = 1.78^{+0.35}_{-0.32}$ and $\Gamma = 1.74^{+0.34}_{-0.31}$, and intrinsic column densities of $N_{\text{H,host}} = 5.10^{+3.07}_{-2.29} \times 10^{22} \text{ cm}^{-2}$ (90 per cent confidence; C-stat = 114 for 155 degrees of freedom) and $N_{\text{H,host}} = 7.31^{+4.58}_{-3.36} \times 10^{22} \text{ cm}^{-2}$ (90 per cent confidence; C-stat = 114 for 155 degrees of freedom) for the LMC-like and SMC-like absorbers, respectively. The X-ray light curve and spectrum is shown in Figs 1 and 4. The XRT data and products were made available by the UK *Swift* Science Data Centre (UKSSDC; Evans et al. 2007, 2009). The data were converted from unabsorbed flux into flux density at 2 keV using the photon index of $\Gamma = 1.83$ we obtained from the spectral analysis using a Solar metallicity absorber.

3 CAN WE CLASSIFY GRB140713A AS A DARK BURST?

One criterion to determine if a GRB is indeed dark was proposed by Jakobsson et al. (2004). They reported that an optical-to-X-ray spectral index $\beta_{\text{OX}} < 0.5$ at 11 h would suggest that the GRB was optically sub-luminous with respect to the relativistic fireball model. The optical flux density is typically measured in the *R* band and the

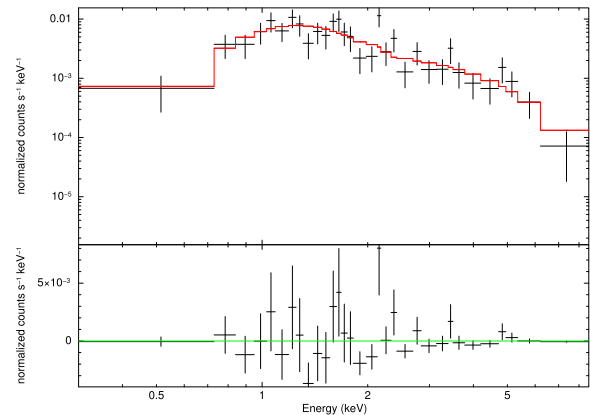


Figure 4. Observed X-ray spectrum of GRB 140713A from *Swift*/XRT excluding the early-time flaring data (see Section 2.4). The absorbed power-law model (red) was created using a Solar metallicity absorber.

Table 3. Spectral information using the optical upper limits and X-ray fluxes to determine if GRB 140713A was dark using the thresholds described in Section 3.

Filter	β_{OX}	$\beta_{\text{OX}} - \beta_{\text{X}}$
<i>r</i>	< 0.20	< -0.30
<i>i</i>	< 0.26	< -0.24
<i>z</i>	< 0.37	< -0.13

X-ray flux density at 2 keV. This criterion was expanded to take into account the X-ray spectral information (van der Horst et al. 2009). Their criterion implies that a GRB can be classified as dark when $\beta_{\text{OX}} - \beta_{\text{X}} < -0.5$, where β_{X} is the X-ray spectral index. We conducted a similar test, taking the unabsorbed X-ray flux at ~ 3.5 h (0.1454 d) and converted this into a flux density at 2 keV. We then calculated the spectral index between each optical band and the X-ray flux at 2 keV. We find $\beta_{\text{OX}} < 0.5$ in all bands, well below the dark GRB threshold put forward by Jakobsson et al. 2004. With $\beta_{\text{X}} = 0.83^{+0.37}_{-0.33}$ (90 per cent confidence) we find that GRB 140713A could also tentatively be classified as a dark GRB via the threshold described in van der Horst et al. (2009). The results using both criteria are seen in Table 3.

4 BROAD-BAND AFTERGLOW MODELLING

4.1 Modelling method

To investigate the origin of the optical darkness of GRB 140713A, we required an estimation of the optical flux we should expect to observe. Extrapolating the X-ray spectral index back to optical wavelengths implied that we should have observed an optical flux $\gtrsim 1$ order of magnitude brighter than the observed limits. To further investigate this discrepancy, we modelled the afterglow data using the software package BOXFIT following the method described in van Eerten, van der Horst & MacFadyen (2012). BOXFIT utilizes the results of compressed radiative transfer hydrodynamic simulations to estimate the parameters of the expanding shock front and surrounding medium of a GRB using the downhill simplex method (Nelder & Mead 1965) optimized with simulated annealing (Kirkpatrick, Gelatt & Vecchi 1983). Using BOXFIT as an alternative to the classical, analytical synchrotron models (i.e. Granot & Sari 2002) allows us to fully compare the multiwavelength

Table 4. The model parameter ranges for the afterglow model fitting.

Parameter	Min	Initial	Max
z^a	–	0.935	–
d_L^a (cm)	–	1.92×10^{28}	–
E_{ISO} (erg)	10^{47}	10^{53}	10^{56}
n (cm^{-3})	10^{-5}	1.0	10^5
$\theta_{j/2}$ (rad)	0.01	0.1	0.5
θ_{obs}^a (rad)	–	0	–
p	1.0	2.0	3.0
$\bar{\epsilon}_e$	10^{-5}	0.1	1.0
ϵ_B	10^{-10}	10^{-5}	1.0
ξ_N^a	–	1.0	–

^aThese parameters were frozen for the modelling. As we ran the models assuming the GRB was observed on-axis ($\theta_{\text{obs}} = 0$), we set the azimuthal and radial resolution parameters to the recommended on-axis values of 1 and 1000, respectively.

data across a variety of times where the dynamical regimes of the afterglow change. BOXFIT models the afterglow from a single, initial injection of energy; we therefore omitted times for which flaring was observed in the X-ray data (see Section 2.4).

The afterglow model we used has nine parameters and is subsequently referred to as Φ :

$$\Phi = [E_{\text{ISO}}, n, \theta_{j/2}, \theta_{\text{obs}}, p, \epsilon_e, \epsilon_B, \xi_N, z], \quad (2)$$

where E_{ISO} is the equivalent isotropic energy output of the blast-wave, n is the circumburst particle number density at a distance of 10^{17} cm, $\theta_{j/2}$ is the jet half-opening angle, θ_{obs} is the observer angle with respect to the jet-axis, p is the electron energy distribution index, ϵ_e and ϵ_B are the fractions of the internal energy in the electrons and shock-generated magnetic field, ξ_N is the fraction of electrons that are accelerated, and z represents the redshift. We assume a standard Λ CDM cosmology where $H_0 = 68 \text{ km s}^{-1} \text{ Mpc}^{-1}$ and $\Omega_M = 0.31$ (Planck Collaboration XIII 2016), and calculate the corresponding luminosity distance, d_L , from the redshift using the method described in Wright (2006).

Three of our nine model parameters – z , and therefore d_L , θ_{obs} , and ξ_N – are kept fixed. We justify these choices for the following reasons. The redshift, z , represents the distance to the GRB and is taken as the redshift of the host galaxy. For θ_{obs} we assume that we observed the GRB on-axis, and we adopted $\xi_N = 1$. This is to remove parameter degeneracies associated with these parameters – we do not have enough data to fully investigate the additional behaviour of these parameters. Our parameter ranges can be found in Table 4.

Fig. 1 highlights that the late-time X-ray temporal slope was shallow; $-0.78(\pm 0.09)$. For a rough estimate of p , we assume that the X-ray band is above the synchrotron cooling break frequency, which is most commonly observed at these times (Curran et al. 2010; Ryan et al. 2015), and use the following closure relations from Zhang & Mészáros (2004): the temporal relation $F_\nu \propto t^{(2-3p)/4}$ and the spectral relation $F_\nu \propto \nu^{-p/2}$ – to estimate p . We estimate from these relations that $1.6 < p < 1.8$ and $1.0 < p < 2.4$ for the temporal and spectral data, respectively. These values suggest that the underlying electron distribution may be very low, i.e. $p < 2$. In light of this, we modified BOXFIT to allow fits where $p < 2$ by replacing ϵ_e with $\bar{\epsilon}_e$, where $\bar{\epsilon}_e = \epsilon_e(p-2)/(p-1)$ (Granot & Sari 2002).

We ran BOXFIT for two different circumburst density environments – a homogeneous medium (subsequently labelled as ISM) and a stellar wind environment where the density decreases as r^{-2} ,

with r the distance of the shock to the centre of the stellar explosion. This allows us to test the significance of the environments on the best-fitting models. The stellar wind environment was run under the medium-boosted wind setting of BOXFIT. We obtained the global best fit (i.e. lowest global χ^2) for the data and calculated the partial derivatives around the best-fitting values. We then used a bootstrap Monte Carlo (MC) method by perturbing the data set 10^4 times within the flux errors to investigate the parameter distributions and confidence intervals (see van Eerten et al. 2012 for a full discussion), showing the results in Fig. 5.

4.2 Feasibility of parameter values and choice of environment for optical flux estimation

Fig. 5 shows that all the fitted parameters in our model, for an ISM-like environment, follow relatively normal and lognormal distributions. We see very similar results in the wind environment and both sets of parameter peak (median) and 68 per cent confidence (1σ) values are found in Table 5. There is some degeneracy between parameters, manifesting in the correlations we observe in Fig. 5 (e.g. the positive correlation between E_{iso} and n , and anticorrelation between ϵ_B and n). Fig. 6 shows that our observations and models constrain the self-absorption and peak frequencies fairly well. Even with well-sampled optical light curves there can be correlations between parameters, because of the complexity and interdependence of several observable and physical parameters. However, since the characteristic synchrotron frequencies and peak flux are well constrained, our modelling work will provide a good estimated optical flux of GRB 140713A. When comparing the best-fitting models of the two different circumburst density environments, the ISM fit has a lower global reduced χ^2 statistic, $\chi_{r,\text{ISM}}^2 = 4.21$ compared to $\chi_{r,\text{WIND}}^2 = 4.70$, but this difference is not statistically significant. Both models fail to reproduce several early-time non-detections in the 4.8 and 15.7 GHz light curve, but at these times scintillation is clearly visible in the data and produces significant short-term flux variability. Both environments produce consistent values within 1σ for E_{ISO} , n , $\theta_{j/2}$, $\bar{\epsilon}_e$, and p ; and consistent within 2σ for ϵ_B .

In both the ISM and wind case, our BOXFIT models prefer a large jet half-opening angle ($\theta_{j/2} \sim 0.5$ rad) implying that a jet break would occur at ~ 25 – 30 d post-GRB (calculated using equation 3 in Starling et al. 2009, see also Frail et al. 2001). This is clearly visible in the 4.8 GHz band light curve in Fig. 6. GRBs exhibit a range of jet opening angles; ranging from the narrow ($\theta_{j/2} \lesssim 0.1$ rad; Frail et al. 2001; Ryan et al. 2015) to the wide (e.g. GRB 970508; Frail, Waxman & Kulkarni 2000 or GRB 000418; Panaitescu & Kumar 2002), with our jet half-opening angle estimation comfortably sitting within the distribution. Both circumburst environments also preferred a scenario with a hard electron energy distribution with $p \sim 1.85$. Although low p values for these two environments have been derived for other GRBs as well, they are in the tails of GRB parameter distributions (e.g. Curran et al. 2010; Ryan et al. 2015).

With the hard electron energy distribution ($p < 2$) preferred by the afterglow modelling, we exercised caution when interpreting the physical meaning of $\bar{\epsilon}_e$ – introduced to allow BOXFIT to model fits where $p < 2$. For $p > 2$ where one can fit for ϵ_e , you can simply estimate the energy of the shocked electrons from the following relation:

$$E_e = \epsilon_e E_{\text{int}}, \quad (3)$$

where E_e is the energy density of the shocked electrons and E_{int} is the energy density of the post-shock fluid. However, as we had a

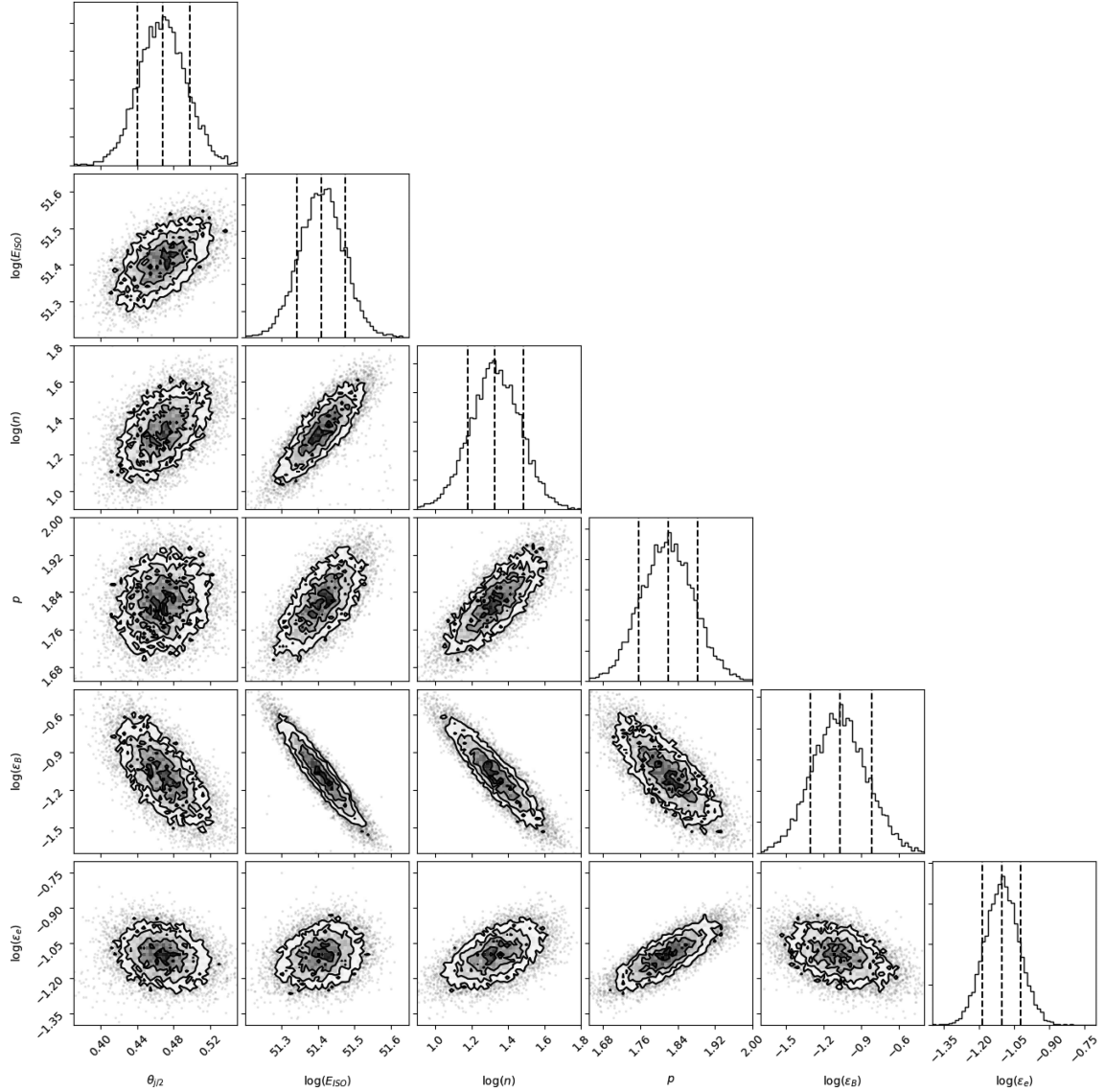


Figure 5. Multidimensional projections of the parameter distributions derived using the MC bootstrap analysis around the BOXFIT ISM best-fitting values. The peak of the distributions and 68 per cent confidence intervals are shown.

Table 5. The best-fitting parameter values derived from our MC analysis for two different circumburst density environments. The values quoted are the peak (median) of the MC distribution and 68% (1σ) confidence intervals. The circumburst density is measured at a distance of 10^{17} cm.

Environment	E_{ISO} (ergs)	n (cm^{-3})	$\theta_{j/2}$ (rad)	θ_{obs}^a (rad)	p	$\bar{\epsilon}_e$	ϵ_B	ξ_N^a	χ_r^2
ISM	$2.57_{-0.33}^{+0.40} \times 10^{51}$	$21.4_{-5.8}^{+8.4}$	$0.47(\pm 0.03)$	0	$1.82(\pm 0.06)$	$7.88_{-1.28}^{+1.42} \times 10^{-2}$	$8.30_{-3.30}^{+5.60} \times 10^{-2}$	1	4.21
Wind	$2.09_{-0.25}^{+0.32} \times 10^{51}$	$22.0_{-3.1}^{+6.8}$	$0.51_{-0.03}^{+0.04}$	0	$1.85_{-0.05}^{+0.06}$	$5.64_{-1.06}^{+1.37} \times 10^{-2}$	$2.80_{-1.01}^{+1.36} \times 10^{-1}$	1	4.70

best fit where $p < 2$ we had to account for the upper energy cut-off of the electron energy distribution by using the following relation:

$$E_e = \bar{\epsilon}_e E_{\text{int}} \frac{(p-1)}{(p-2)} \left[1 - \left(\frac{\gamma_M}{\gamma_m} \right)^{2-p} \right], \quad (4)$$

where γ_M and γ_m represent the maximum (cut-off) and minimum Lorentz factors accounting for the cut-off with $\bar{\epsilon}_e$ defined as before (Granot & Sari 2002). For further details on $\bar{\epsilon}_e$, see Appendix A. If we assume values of $\gamma_M \sim 10^7$ and $\gamma_m \sim 10^3$, and take the derived

values for p and $\bar{\epsilon}_e$ for both the ISM and wind environments from Table 5, we find that the typical energy densities from equation (3) are a factor of ~ 15 – 20 lower than for equation (4). This is not surprising given the form of equation (4) – as $p \rightarrow 2$ the energy of the electrons using the above relation asymptotically scales towards infinity, resulting in energy efficiencies, $\epsilon_e > 1$, which are not physical. In Section 4, we discussed our model parameter selection, including fixing $\xi_N = 1$ as we do not have sufficient data to explore the degeneracy of this parameter with the other parameters. A linear decrease in ξ_N would result in a linear increase

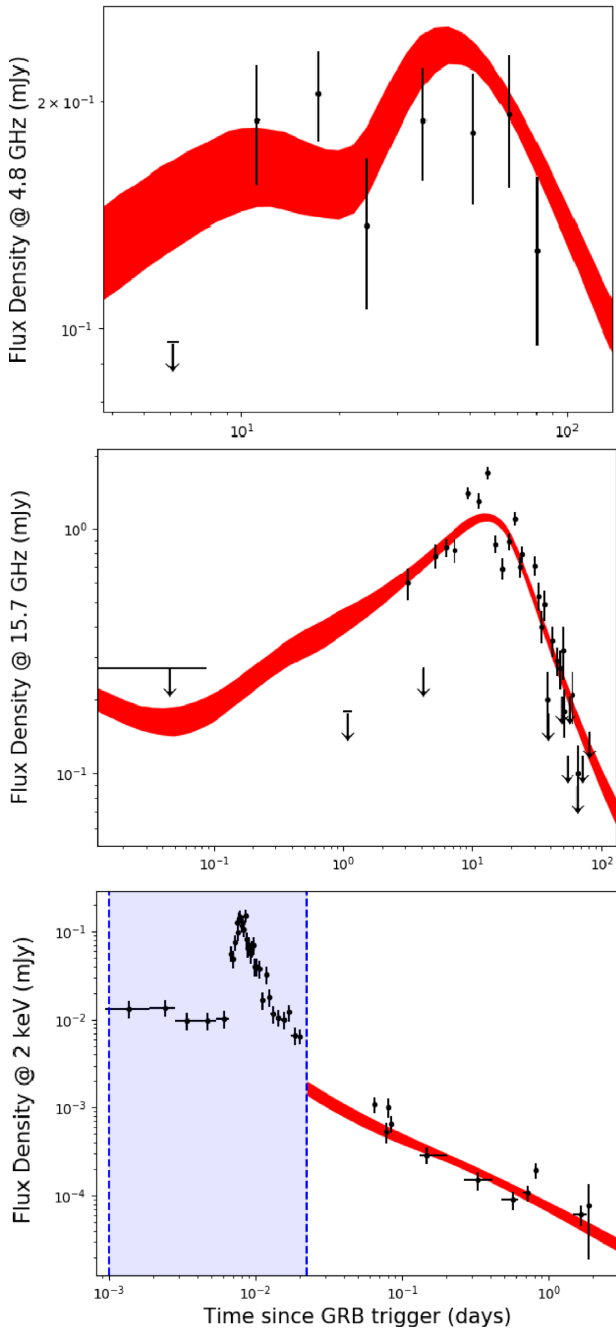


Figure 6. Multiwavelength light curves of GRB 140713A for an ISM-like environment. The red region represents the 68 per cent confidence region. This was derived from generating model light curves from a random sample of 500 parameter sets, found using the MC bootstrap. We then plotted the model fluxes between the 16th and 84th percentiles (the distributions of fluxes in each model time bin were normal). The shaded blue region in the bottom window represents the X-ray flare that was omitted from the modelling.

in energy, E_{ISO} but simultaneous linear decreases in both ϵ_e and ϵ_B (Eichler & Waxman 2005). Therefore, if we had set a value of $\xi_N = 0.1$, we would have seen an increase in the available energy budget to $E_{\text{ISO}} \sim 10^{52}$ ergs but also would have seen $\epsilon_B \sim 0.01$ and $\epsilon_e \sim 0.1$ for both the ISM and wind environments, in which case ϵ_e would be physical.

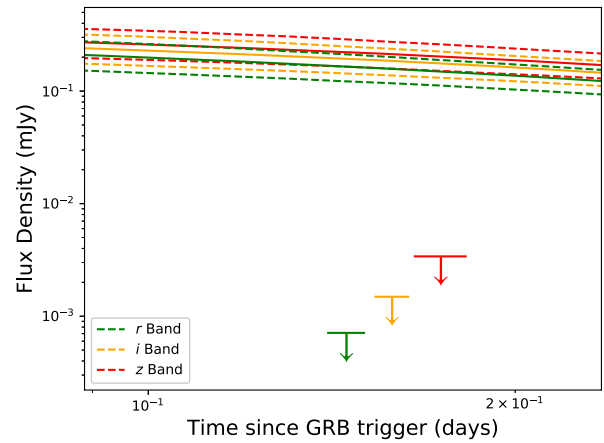


Figure 7. Optical light curves of the r (green), i (orange), and z (red) bands for an ISM-like model. The solid lines represent the 50th percentile (median) values and the dashed lines represent the 16th and 84th percentile values (the 68 per cent confidence intervals).

5 OPTICAL DARKNESS

The temporal and spectral behaviour of GRB 140713A in the gamma-ray, X-ray, and radio regimes are very typical of GRB afterglows. Our optical observations were taken at such early times and with a sensitivity that a counterpart should have been detected. In Section 2.3, we discussed observations of an associated host galaxy in a number of optical and near-infrared bands. The 1D spectrum shows two strong emission lines – $[\text{O II}]\lambda 3727$ and $[\text{O III}]\lambda 5007$ – both occurring at the same redshift, $z = 0.935$. We therefore rule out that the optical darkness is due to low intrinsic luminosity of the GRB or a high-redshift nature.

As the physical parameters of both environments were very similar, but the ISM environment had a smaller χ_r^2 derived from our BOXFIT modelling, we used the ISM derived parameters to estimate the optical flux in the r , i , and z bands. We randomly sampled 500 parameter sets from the 10^4 sets derived from the MC bootstrap and produced light curves in the r , i , and z bands. The flux values for each of the 500 light-curve models, in each time bin, were found to follow lognormal distributions (see Appendix B for examples). We therefore plotted the 16th, 50th, and 84th percentiles of each time bin to illustrate the most-probable flux and 68 per cent confidence intervals from our model (see Fig. 7). We also quote these percentiles as our results in Table 6. These were then compared to the expected fluxes to our observational upper limits. The estimated flux in the r , i , and z bands are $\gtrsim 2$ orders of magnitude above the upper limits (Table 6). The estimated flux values from Fig. 7 confirm that optical observations were promptly taken and should have led to detections of the GRB 140713A counterpart. The remaining plausible explanation for the optical darkness of this GRB is optical extinction in the line of sight towards the source.

The estimated optical flux values are given in Table 6 and allowed us to uncover the potential source of optical extinction. We used the BOXFIT derived fluxes to estimate lower limits on the extinction in the r , i , and z bands, ranging from 4.1 to 5.7 mag. We used Milky Way-like ($R_V = 3.1$; Cardelli, Clayton & Mathis 1989), LMC-like ($R_V = 3.41$; Gordon et al. 2003) and SMC-like ($R_V = 2.74$; Gordon et al. 2003) extinction models to derive the required host extinction (A_V^{host}) after transforming the observed bands into

Table 6. Table containing the observed optical limits, BOXFIT fluxes, required level of extinction and derived host extinctions (A_V^{host}) using Milky Way-like, LMC-like, and SMC-like extinction models. The lower limits shown for the required level of extinction were calculated from the magnitude difference between the observational upper limit and the faintest estimate from BOXFIT at the given wavelength (i.e. 18.6 mag for r band). Host extinction values have been corrected for Galactic extinction $-E(B - V) = 0.05$ mag; $A_V^{\text{host}} = 0.16$ mag; (Schlafly & Finkbeiner 2011). Quoted errors on BOXFIT fluxes at 68 per cent confidence.

Filter	ΔT (d)	Mag (AB)	Flux (mJy)	BOXFIT flux (mJy)	BOXFIT Mag (mag)	Req Ext (mag)	Galactic A_V^{host} (mag)	LMC A_V^{host} (mag)	SMC A_V^{host} (mag)
r	0.15	> 24.3	$< 7.1 \times 10^{-4}$	$0.17_{-0.04}^{+0.05}$	18.3(± 0.3)	>5.7	>3.1	>3.2	>2.9
i	0.16	> 23.5	$< 1.5 \times 10^{-3}$	$0.19(\pm 0.05)$	18.2(± 0.3)	>5.0	>3.2	>3.3	>3.0
z	0.17	> 22.6	$< 3.4 \times 10^{-3}$	$0.20_{-0.05}^{+0.06}$	$18.1_{-0.2}^{+0.4}$	>4.1	>3.2	>3.2	>3.1

their corresponding wavelengths in rest frame of the host galaxy at $z = 0.935$. We then subtracted the Galactic extinction contribution $E(B - V)^{\text{Gal}} = 0.05$ mag. The three extinction models produced similar results; see Table 6. The most constraining limit from the Milky Way-like extinction model was $A_V^{\text{host}} > 3.2$ mag equivalent to $E(B - V)^{\text{host}} > 1.0$ mag.

We independently estimated the host extinction level using the relationship between X-ray absorption and optical extinction (Gorenstein 1975; Predehl & Schmitt 1995). A more recent study published in 2009 constrained this relationship to N_{H} (cm^{-2}) = $2.21(\pm 0.09) \times 10^{21} A_V$ (Güver & Özel 2009). In Section 2.4, we estimated the intrinsic hydrogen column density of GRB 140713A, $N_{\text{H,host}} = 2.6_{-1.12}^{+1.48} \times 10^{22} \text{cm}^{-2}$ (90 per cent confidence, assuming Solar metallicity absorber). We estimate the expected optical host extinction based on the relation between extinction and X-ray column density for the Milky Way, LMC, and SMC in Güver & Özel (2009). We calculate that the extinction for the host is $A_V^{\text{host}} = 11.6_{-5.3}^{+7.5}$ mag (90 per cent confidence), equivalent to $E(B - V)^{\text{host}} = 3.7_{-1.7}^{+2.4}$ mag for the Milky Way-like extinction model. Combining the SMC-like and LMC-like absorber intrinsic column densities derived in Section 2.4 with the relation from Güver & Özel (2009) results in estimated host extinction values of $A_V = 23.1_{-10.4}^{+13.9}$ mag and $A_V = 33.1_{-15.2}^{+20.7}$ mag, respectively. Our estimated host extinction using the hydrogen column density is in good agreement with the extinction limits calculated from the BOXFIT generated light curves, and suggests that the source of the optical extinction is due to dust within the host galaxy.

5.1 Comparing the extinction of dark GRBs

Only a handful of dark GRBs with accompanying radio data have been observed. The explosion and circumburst properties of these GRBs were compared in Zauderer et al. (2013). Table 7 summarizes the estimated host extinction of all of these bursts to date and GRB 140713A from this investigation.

The required host extinction values vary significantly in this small sample from modest ($A_V^{\text{host}} \lesssim 1.5$ mag) to high ($A_V^{\text{host}} > 8.2$ mag) and GRB 140713A is typical among the other dark GRBs. Interestingly, at least five of the seven GRBs exhibit required extinctions of >3 mag. The levels of extinction are in good agreement with larger sample studies of optically dark GRB host galaxies (Perley et al. 2009, 2013). The results therefore suggest that the optical extinction of a significant fraction of dark GRBs is at least partially due to dust-obscuration in the host galaxy, either in the local environment of the progenitor or throughout the galaxy.

Table 7. Required host extinction values for a number of dark GRBs with complementary radio data. All extinctions are quoted directly from their respective sources unless otherwise stated and are displayed in the rest frame of the host.

GRB name	A_V^{host} (mag)	Reference
970828	>3.8	Djorgovski et al. (2001)
000210	0.9–3.2	Piro et al. (2002)
020809	0.6–1.5	Jakobsson et al. (2005)
051022	>8.2 ^a	Rol et al. (2007)
110709B	>5.3	Zauderer et al. (2013)
111215A	>7.5	van der Horst et al. (2015)
140713A	>3.2	This work

Note. ^aMost constraining limit derived using their quoted J -band extinction in the host rest frame ($A_J^{\text{host}} > 2.3$ mag) and transforming this into the V -band extinction assuming a Milky Way-like extinction curve.

6 CONCLUSIONS

The afterglow of GRB 140713A was detected in both the X-ray and radio bands but not seen to deep limits in optical and near-infrared observations. We measured the likely host galaxy redshift of $z = 0.935$, allowing us to rule out a high-redshift origin. We investigated the origin of optical darkness in this GRB utilizing hydrodynamical jet simulations through the modelling software BOXFIT. We produced a number of models in both an ISM-like and wind circumburst environment to estimate what level of optical flux we could have expected from the afterglow. The models provided good fits to the observed data, preferring a wide jet half-opening angle ($\theta_{j/2} \sim 0.5$ rad) and a hard electron energy distribution ($p \sim 1.85$). Crucially, the models predicted that the observed optical afterglow should have been ~ 2 orders of magnitude brighter than our observed upper limits and therefore easily observable, ruling out an intrinsically low-luminosity optical afterglow. From the discrepancy between the estimated optical flux values and our observations we estimated that we require an extinction $A_V^{\text{host}} > 3.2$ mag in the rest frame of the host. The host optical extinction, inferred from the hydrogen column density measured in the X-ray afterglow spectra data, was consistent with our requirements. We therefore conclude that the optical darkness of GRB 140713A is most likely caused by a large amount of extinction either in the local vicinity of the progenitor or throughout the host galaxy.

ACKNOWLEDGEMENTS

We greatly appreciate the support from the WSRT and AMI staff in their help with scheduling and obtaining these observations.

The WSRT is operated by ASTRON (Netherlands Institute for Radio Astronomy) with support from the Netherlands foundation for Scientific Research. The AMI arrays are supported by the University of Cambridge and the STFC. Some of the data presented herein were obtained at the W.M. Keck Observatory, which is operated as a scientific partnership among the California Institute of Technology, the University of California and the National Aeronautics and Space Administration (NASA); the Observatory was made possible by the generous financial support of the W.M. Keck Foundation. The Nordic Optical Telescope is operated on the island of La Palma by the Nordic Optical Telescope Scientific Association in the Spanish Observatorio del Roque de los Muchachos of the Instituto de Astrofísica de Canarias. This work made use of data supplied by the UK Swift Science Data Centre at the University of Leicester. ABH is supported by a Science and Technology Facilities Council (STFC) studentship. RLCS, KW and NRT acknowledge support from STFC. GA acknowledges the support of the European Research Council Advanced Grant 267697 ‘4 Pi Sky: Extreme Astrophysics with Revolutionary Radio Telescopes’. GA is the recipient of an Australian Research Council Discovery Early Career Researcher Award (project number DE180100346) funded by the Australian Government. We thank the referee for their constructive feedback, which improved the paper.

REFERENCES

- Anderson G. E., Fender R. P., Staley T. D., van der Horst A. J., 2014, *GCN Circ.*, 16603
- Anderson G. E. et al., 2018, *MNRAS*, 473, 1512
- Arnaud K. A., 1996, in Jacoby G. H., Barnes J., eds, *ASP Conf. Ser. Vol. 101*, *Astronomical Data Analysis Software and Systems V*. Astron. Soc. Pac., San Francisco, p. 17
- Barthelmy S. D. et al., 2005, *Space Sci. Rev.*, 120, 143
- Beardmore A. P., Evans P. A., Goad M. R., Osborne J. P., 2014, *GCN Circ.*, 16585
- Blain A. W., Natarajan P., 2000, *MNRAS*, 312, L35
- Bloom J. S., Kulkarni S. R., Djorgovski S. G., 2002, *AJ*, 123, 1111
- Burrows D. N. et al., 2005, *Space Sci. Rev.*, 120, 165
- Burrows D. N. et al., 2008, preprint ([arXiv:0803.1844](https://arxiv.org/abs/0803.1844))
- Cano Z., Malesani D., Nielsen M., 2014, *GCN Circ.*, 16587
- Cardelli J. A., Clayton G. C., Mathis J. S., 1989, *ApJ*, 345, 245
- Castro-Tirado A. J. et al., 2007, *A&A*, 475, 101
- Castro-Tirado A. J., Jeong S., Gorosabel J., Reverte D., 2014, *GCN Circ.*, 16602
- Chandra P., Nayana A. J., 2014, *GCN Circ.*, 16641
- Contini T. et al., 2012, *A&A*, 539, A91
- Cucchiara A. et al., 2011, *ApJ*, 736, 7
- Curran P. A., Evans P. A., de Pasquale M., Page M. J., van der Horst A. J., 2010, *ApJ*, 716, L135
- Dickinson C. et al., 2004, *MNRAS*, 353, 732
- Djorgovski S. G., Frail D. A., Kulkarni S. R., Bloom J. S., Odewahn S. C., Diercks A., 2001, *ApJ*, 562, 654
- Eichler D., Waxman E., 2005, *ApJ*, 627, 861
- Evans P. A. et al., 2007, *A&A*, 469, 379
- Evans P. A. et al., 2009, *MNRAS*, 397, 1177
- Frail D. A., Waxman E., Kulkarni S. R., 2000, *ApJ*, 537, 191
- Frail D. A. et al., 2001, *ApJ*, 562, L55
- Fynbo J. P. U. et al., 2009, *ApJS*, 185, 526
- Gehrels N. et al., 2004, *ApJ*, 611, 1005
- Gordon K. D., Clayton G. C., Misselt K. A., Landolt A. U., Wolff M. J., 2003, *ApJ*, 594, 279
- Gorenstein P., 1975, *ApJ*, 198, 95
- Granot J., Sari R., 2002, *ApJ*, 568, 820
- Greiner J. et al., 2011, *A&A*, 526, A30
- Groot P. J. et al., 1998, *ApJ*, 493, L27
- Güver T., Özel F., 2009, *MNRAS*, 400, 2050
- Jaeger S., 2008, in Argyle R. W., Bunclark P. S., Lewis J. R., eds, *ASP Conf. Ser. Vol. 394*, *Astronomical Data Analysis Software and Systems XVII*. Astron. Soc. Pac., San Francisco, p. 623
- Jakobsson P., Hjorth J., Fynbo J. P. U., Watson D., Pedersen K., Björnsson G., Gorosabel J., 2004, *ApJ*, 617, L21
- Jakobsson P. et al., 2005, *ApJ*, 629, 45
- Jordi K., Grebel E. K., Ammon K., 2006, *A&A*, 460, 339
- Kirkpatrick S., Gelatt C. D., Vecchi M. P., 1983, *Science*, 220, 671
- Kumar P., Zhang B., 2015, *Phys. Rep.*, 561, 1
- Mangano V., Barthelmy S. D., Chester M. M., Cummings J. R., Kennea J. A., Sbarufatti B., 2014, *GCN Circ.*, 16581
- Melandri A. et al., 2012, *MNRAS*, 421, 1265
- Nelder J. A., Mead R., 1965, *Comput. J.*, 7, 308
- Oke J. B. et al., 1995, *PASP*, 107, 375
- Panaiteanu A., Kumar P., 2002, *ApJ*, 571, 779
- Perley D. A. et al., 2009, *AJ*, 138, 1690
- Perley D. A. et al., 2013, *ApJ*, 778, 128
- Perley D. A. et al., 2016, *ApJ*, 817, 7
- Perrott Y. C. et al., 2013, *MNRAS*, 429, 3330
- Piran T., 1999, *Phys. Rep.*, 314, 575
- Piro L. et al., 2002, *ApJ*, 577, 680
- Planck Collaboration XIII, 2016, *A&A*, 594, A13
- Predehl P., Schmitt J. H. M. M., 1995, *A&A*, 293, 889
- Ramirez-Ruiz E., Trentham N., Blain A. W., 2002, *MNRAS*, 329, 465
- Rees M. J., Meszaros P., 1994, *ApJ*, 430, L93
- Rol E., Wijers R. A. M. J., Kouveliotou C., Kaper L., Kaneko Y., 2005, *ApJ*, 624, 868
- Rol E. et al., 2007, *ApJ*, 669, 1098
- Roming P. W. A. et al., 2005, *Space Sci. Rev.*, 120, 95
- Roming P. W. A. et al., 2009, *ApJ*, 690, 163
- Ryan G., van Eerten H., MacFadyen A., Zhang B.-B., 2015, *ApJ*, 799, 3
- Sault R. J., Teuben P. J., Wright M. C. H., 1995, in Shaw R. A., Payne H. E., Hayes J. J. E., eds, *ASP Conf. Ser. Vol. 77*, *Astronomical Data Analysis Software and Systems IV*. Astron. Soc. Pac., San Francisco, p. 433
- Schady P., 2017, *R. Soc. Open Sci.*, 4, 170304
- Schady P. et al., 2012, *A&A*, 537, A15
- Schlaflly E. F., Finkbeiner D. P., 2011, *ApJ*, 737, 103
- Staley T. D., Anderson G. E., 2015a, *Astrophysics Source Code Library*, record ascl:1502.017
- Staley T. D., Anderson G. E., 2015b, *Astrophysics Source Code Library*, record ascl:1504.005
- Staley T. D., Anderson G. E., 2015c, *Astron. Comput.*, 13, 38
- Staley T. D., Fender R., 2016, preprint ([astro-ph/1606.03735](https://arxiv.org/abs/1606.03735))
- Staley T. D. et al., 2013, *MNRAS*, 428, 3114
- Stamatikos M. et al., 2014, *GCN Circ.*, 16584
- Starling R. L. C. et al., 2009, *MNRAS*, 400, 90
- Swinbank J. D. et al., 2015, *Astron. Comput.*, 11, 25
- Tan G. H., 1991, in Cornwell T. J., Perley R. A., eds, *ASP Conf. Ser. Vol. 19*, *IAU Colloq. 131: Radio Interferometry. Theory, Techniques, and Applications*. Astron. Soc. Pac., San Francisco, p. 42
- Tanvir N. R. et al., 2009, *Nature*, 461, 1254
- van der Horst A. J., Kouveliotou C., Gehrels N., Rol E., Wijers R. A. M. J., Cannizzo J. K., Racusin J., Burrows D. N., 2009, *ApJ*, 699, 1087
- van der Horst A. J. et al., 2015, *MNRAS*, 446, 4116
- van Eerten H., 2018, *Int. J. Mod. Phys. D*, 27, 1842002–314
- van Eerten H., van der Horst A., MacFadyen A., 2012, *ApJ*, 749, 44
- Willingale R., Starling R. L. C., Beardmore A. P., Tanvir N. R., O’Brien P. T., 2013, *MNRAS*, 431, 394
- Wright E. L., 2006, *PASP*, 118, 1711
- Zauderer B. A. et al., 2013, *ApJ*, 767, 161
- Zhang B.-B., 2014, *GCN Circ.*, 16590
- Zhang B., Mészáros P., 2004, *Int. J. Mod. Phys. A*, 19, 2385
- Zwart J. T. L. et al., 2008, *MNRAS*, 391, 1545

APPENDIX A: INTERPRETATION OF A HARD ELECTRON ENERGY DISTRIBUTION

We assume a power-law accelerated electron number density according to $n_e(\gamma_e) = C\gamma_e^{-p}$ between lower cut-off γ_m and upper cut-off γ_M , where γ_e the Lorentz factor of individual electrons in the frame locally co-moving with the fluid, and C a constant of proportionality constrained by the total number density of electrons. Following Granot & Sari (2002), we use $\bar{\epsilon}_e$ rather than ϵ_e as a fit parameter to model the fraction of available blast wave energy that resides in the accelerated electron population:

$$\gamma_m \equiv \frac{\bar{\epsilon}_e E_{\text{int}}}{\xi_N n m_e c^2} \equiv \frac{(p-2)}{(p-1)} \frac{\epsilon_e E_{\text{int}}}{\xi_N n m_e c^2}. \quad (\text{A1})$$

Here, E_{int} is the internal post-shock energy density of the fluid and n its post-shock number density. The upper cut-off γ_M reflects the balance between shock-acceleration time and synchrotron loss time.

We do not account for γ_M when generating light curves, given that its observational signature (an exponential drop in flux) will lie orders of magnitude above the X-ray band for reasonable model parameter values. If $p > 2$, γ_M can also be ignored when inferring the total energy available to electrons E_e from our fit result for $\bar{\epsilon}_e$, according to $E_e = \epsilon_e E_{\text{int}} = \bar{\epsilon}_e E_{\text{int}}(p-1)/(p-2)$.

More generally, when allowing for $p < 2$ as well, we have

$$E_e = C m_e c^2 \int_{\gamma_m}^{\gamma_M} d\gamma_e \gamma_e^{1-p} \approx \begin{cases} \gamma_m^2 n_e(\gamma_m) m_e c^2 / (p-2), & p > 2, \\ \gamma_m^2 n_e(\gamma_m) m_e c^2 \ln[\gamma_M/\gamma_m], & p = 2, \\ \gamma_M^2 n_e(\gamma_M) m_e c^2 / (2-p), & p < 2. \end{cases} \quad (\text{A2})$$

Here, the $p > 2$ and $p < 2$ cases have their energy estimate dictated by γ_m and γ_M , respectively (with γ_M and γ_m , respectively, being ignored in the preceding equations). If all terms are accounted for, and $E_{e,\text{old}}$ is our inferred electron energy when ignoring γ_M , the actual value for E_e is given by the following relation:

$$E_e = E_{e,\text{old}} \left[1 - \left(\frac{\gamma_M}{\gamma_m} \right)^{p-2} \right] = \bar{\epsilon}_e \frac{(p-1)}{(p-2)} E_{\text{int}} \left[1 - \left(\frac{\gamma_M}{\gamma_m} \right)^{p-2} \right]. \quad (\text{A3})$$

APPENDIX B: OPTICAL FLUX DISTRIBUTIONS DERIVED FROM THE MC SAMPLES

Fig. B1 represents the flux distributions from the 500 randomly sampled parameter set light curves discussed in Section 4. The time bin of the displayed fluxes in the r , i , and z bands corresponds to the times of the observations in those filters (see Table 6). The distributions are clearly lognormal so the median flux values and 68 per cent confidence intervals can be quoted using the 16th, 50th, and 84th percentiles.

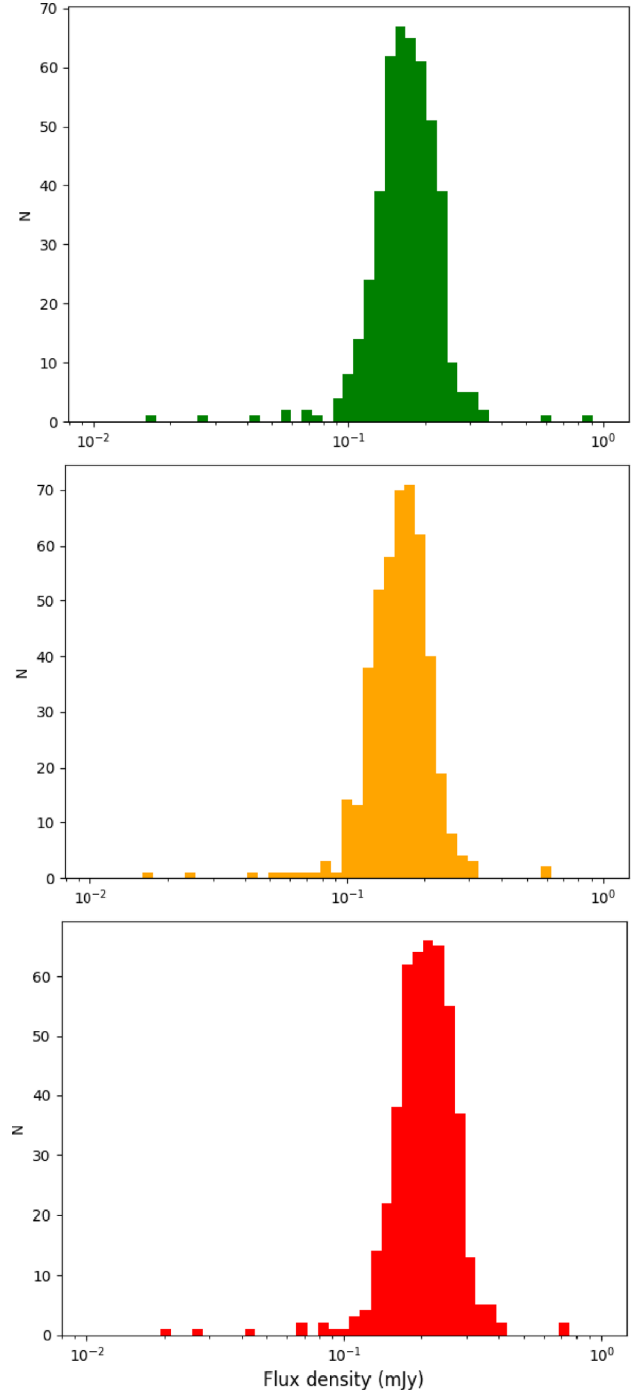


Figure B1. Optical flux distribution of the r (green), i (orange), and z (red) bands. The time bins represented in each window are 0.15 d for r band, 0.16 d for i band, and 0.17 d for z band.

This paper has been typeset from a $\text{\TeX}/\text{\LaTeX}$ file prepared by the author.